Engineering 14 (2022) 86–93

Contents lists available at ScienceDirect

Engineering

journal homepage: www.elsevier.com/locate/eng

Research
Green Chemical Engineering—Article

# Engineering Dual Oxygen Simultaneously Modified Boron Nitride for Boosting Adsorptive Desulfurization of Fuel

Jing Luo [a,b], Yanchen Wei [c], Yanhong Chao [b,d], Chao Wang [a], Hongping Li [a], Jun Xiong [a], Mingqing Hua [a], Huaming Li [a], Wenshuai Zhu [a,b,*]

[a] School of Chemistry and Chemical Engineering & Institute for Energy Research, Jiangsu University, Zhenjiang 212013, China
[b] State Key Laboratory of Heavy Oil Processing, College of Chemical Engineering and Environment, China University of Petroleum (Beijing), Beijing 102249, China
[c] School of Materials Science and Engineering, Jiangsu University, Zhenjiang 212013, China
[d] School of Pharmacy, Jiangsu University, Zhenjiang 212013, China

ARTICLE INFO

*Article history:*
Received 19 March 2020
Revised 6 August 2020
Accepted 7 August 2020
Available online 12 March 2022

*Keywords:*
Polymer-based synthetic strategy
Interior substitution BN
Oxygen doping
Adsorptive desulfurization

ABSTRACT

Oxygen atoms usually co-exist in the lattice of hexagonal boron nitride (h-BN). The understanding of interactions between the oxygen atoms and the adsorbate, however, is still ambiguous on improving adsorptive desulfurization performance. Herein, simultaneously oxygen atom-scale interior substitution and edge hydroxylation in BN structure were constructed via a polymer-based synthetic strategy. Experimental results indicated that the dual oxygen modified BN (BN–2O) exhibited an impressively increased adsorptive capacity about 12% higher than that of the edge hydroxylated BN (BN–OH) fabricated via a traditional method. The dibenzothiophene (DBT) was investigated to undergo multimolecular layer type coverage on the BN–2O uneven surface via π–π interaction, which was enhanced by the increased oxygen doping at the edges of BN–2O. The density functional theory calculations also unveiled that the oxygen atoms confined in BN interior structure could polarize the adsorbate, thereby resulting in a dipole interaction between the adsorbate and BN–2O. This effect endowed BN–2O with the ability to selectively adsorb DBT from the aromatic-rich fuel, thereafter leading to an impressive prospect for the adsorptive desulfurization performance of the fuel. The adsorptive result was in good accordance with Freundlich and pseudo-second-order adsorption kinetics model results. Therefore, the designing of a polymer-based strategy could be also extended to other heteroatom doping systems to enhance adsorptive performance.



## 1. Introduction

Light cycle oil (LCO), an important by-product of the fluid catalytic cracking (FCC) unit in the refinery, needs to be further processed before being used as a fuel due to its high contents of aromatic (up to 90 wt%) and sulfur (up to 4.0 wt%) [1]. The hydrotreating and hydrocracking technologies are the widely utilized protocols to upgrade the LCO to high-quality products by hydrogenating, cracking, and isomerizing the polycyclic aromatic components [2,3]. Nevertheless, the refractory aromatic sulfur in LCO, such as the dibenzothiophene (DBT) and 4,6-dimethyldibenzothiophene (4,6-DMDBT), requires tougher conditions and thusly higher costs to be removed [4]. Consequently, additional desulfurization for the cracking products should be available to reduce the production cost of clean fuel. Nowadays, alternative methods, including oxidative desulfurization [5–10], extractive desulfurization [11,12], and adsorptive desulfurization [13–18], have been developed aiming at the removal of refractory sulfur. Among them, adsorptive desulfurization has attracted extensive attention due to its mild conditions of adsorbing aromatic sulfur compounds, and the highly efficient adsorbent is recognized to be the crucial factor influencing the adsorptive desulfurization performance [18]. In this regard, the adsorptive desulfurization can facilely remove the hydrotreating resided aromatic sulfur, reducing the upgrading cost of LCO (Fig. 1).

Hexagonal boron nitride (h-BN), as a prototypical layered material, has found wide applications in various fields, for instance, catalysis, adsorption, magnetism, ecology, biology, and thermal

* Corresponding author.
*E-mail address:* zhuws@ujs.edu.cn (W. Zhu).

https://doi.org/10.1016/j.eng.2020.08.030

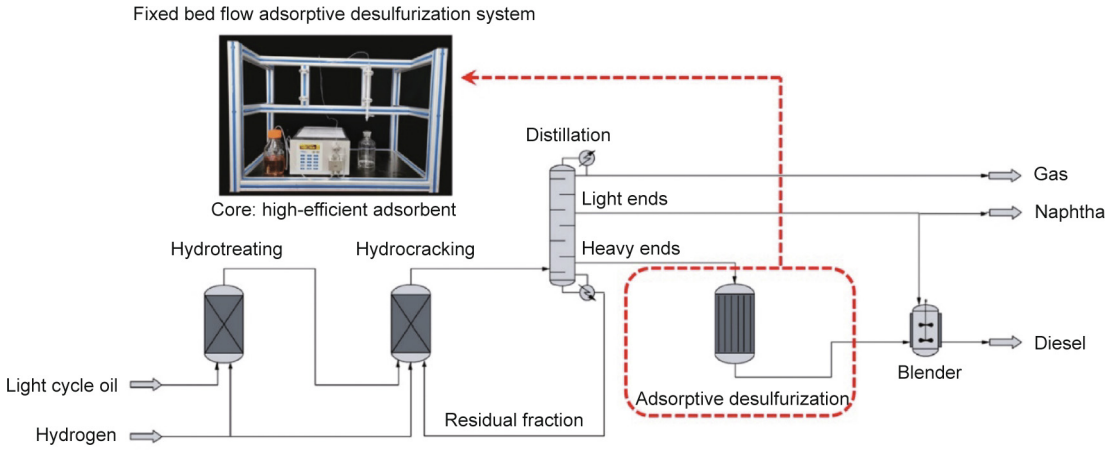


**Fig. 1.** Schematic diagram of the petroleum refining process [1].

conductivity [19–22]. Typically, the design of artificial materials to tune the local atomic structure and electronic structure is of high priority in many fields, for example, oxidation [23,24], supercapacitor [25], electrochemical synthesis [26], adsorption [27,28]. Previous reports show that the electronic and surface structures of BN materials play a significant role in the application (hydrogen storage, adsorptive desulfurization, etc.) [29–32]. Importantly, in contrast to pristine BN, heteroatom-doped BN provides a unique electronic structure and has many distinctive properties, such as excellent catalytic activity [33], impressive electron delocalization effect [34], and high adsorption performance [35,36]. In particular, the oxygen atom-doped BN shows unique properties due to the higher electronegativity of the oxygen atom in comparison with the nitrogen atom. To date, diverse synthetic methods have been utilized in oxygen-doped BN (Table S1 in Appendix A). When oxygen atoms were doped in BN material, a low level of lattice defects could lead to the room-temperature ferromagnetism [37]. And the hybrid boron–nitrogen–oxygen systems with excellent stability can provide enhanced adsorption energies, which ensure them can be employed as the hydrogen storage material [38]. In view of the above considerations, controlling the electronic and surface structures of BN materials is therefore an effective yet straightforward strategy to regulate their adsorptive desulfurization performance.

Recently, Weng et al. [39] proposed that the embedding of oxygen atoms into the BN was a rather practical strategy to tailor the electronic structures, and that the electron-attracting ability of BN could be considerably improved by replacing nitrogen atoms with oxygen atoms. Because of this, the oxygen-doped BN adsorbent exhibited a high adsorption activity through lopsided density characteristics [40]. Previous research mainly focused on enhancing adsorptive desulfurization performance by using oxygen atoms modified BN [41]. However, there have been few reports regarding embedding oxygen atoms into the in-plane lattice of BN or edge hydroxylation modified BN (BN–OH) for the adsorptive desulfurization so far. Thus, oxygen atoms interior substitution coupling with edge hydroxylation is expected to simultaneously alter the electronic structures and thereafter improve the adsorptive ability of BN.

In the present study, we proposed a polymer-based synthetic method to controllably construct atom-scale dual oxygen simultaneously modified BN (BN–2O). The effect of introduced oxygen atoms on electronics, as well as surface structures for adsorptive desulfurization were systematically investigated. It was found that BN–2O had the decent capacity for the adsorptive desulfurization owing to the enhanced π–π interaction caused by its increased oxygen doping at edge structures. Besides, BN–2O also showed an improved selective absorption, for oxygen atoms confined in BN interior structure could polarize the adsorbate, which could result in a dipole interaction between the adsorbate and BN–2O. Moreover, BN–2O exhibited higher adsorptive ability than that of BN–OH due to its unique electronic structure and hierarchically porous structure. This work provides a deep insight into the controllable synthesis of oxygen-doped BN structures for adsorptive desulfurization, and would be warmly expected to the development of heteroatom-doped adsorbent materials.

## 2. Materials and method

### 2.1. Synthesis of BN–2O and BN–OH

Cyanuric chloride ($C_3N_3Cl_3$, 0.02 mol) and melamine ($C_3H_6N_6$, 0.06 mol) were first added in acetonitrile (50 mL) at room temperature, and the mixture was then vigorously stirred for 30 min. Then, the boric acid (0.01 mol) was added into the above solution and kept stirring overnight. Subsequently, the resulting product was obtained after the solution being steamed at 70 °C and calcined at 900 °C for 2 h under the high purity nitrogen flow (200 mL·min$^{-1}$), and denoted as BN–2O (oxygen atom-scale interior substitution and edge hydroxylation, Fig. 2).

BN–OH (edge hydroxylation) was prepared in a similar process to BN–2O without the addition of $C_3N_3Cl_3$.

The reagent source and purity were listed in the supplemental information file in Appendix A.

### 2.2. Characterizations

The morphology of the materials were characterized by a field-emission scanning electron microscope (SEM, JSM-7001F, JEOL, Japan) and transmission electron microscopy (TEM, JEM-2100, JEOL). The X-ray diffraction (XRD) measurements were carried out on a Shimadzu XRD-6100 X-ray diffractometer (Japan) with Cu $K_\alpha$ radiation. $N_2$ adsorption and desorption isotherms were taken on a Micromeritics ASAP 2020 HD88 surface area and porosity analyzer (Micromeritics Instrument Corporation, USA), and the pore size distributions were obtained by the nonlocal density functional theory (NLDFT) calculation. The Fourier transform infrared (FTIR) spectra were collected on a Nicolet Nexus 470 FTIR spectrophotometer (Thermo Electron Corporation, USA). The

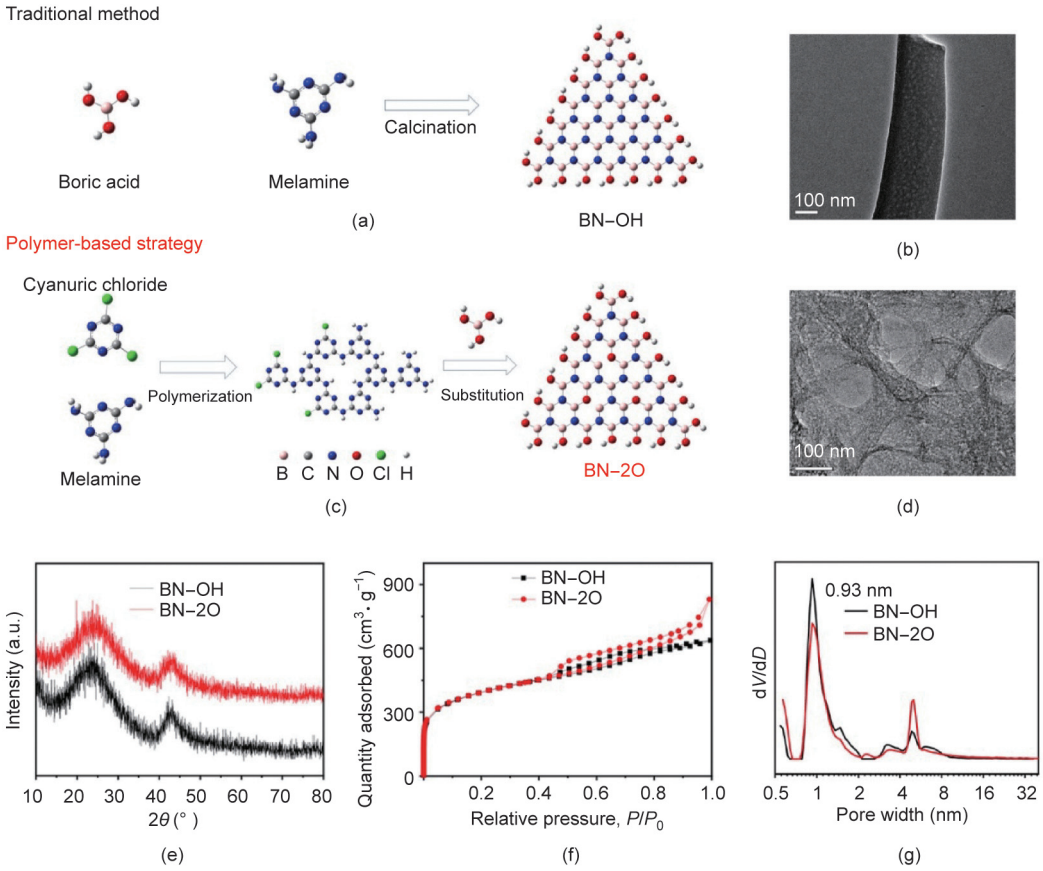


**Fig. 2.** The possible synthesis schematic and TEM images of (a, b) BN–OH and (c, d) BN–2O, respectively; (e) XRD patterns of BN–OH and BN–2O; (f) the $N_2$ adsorption–desorption isotherms; (g) the pore size distribution of BN–OH and BN–2O. a.u.: arbitrary unit.

ultraviolet–visible (UV–Vis) diffuse reflection spectra (DRS) were recorded in a UV-2450 spectrophotometer (Shimadzu Corporation). The X-ray photon spectroscopy (XPS) was performed at a VG MultiLab 2000 spectrometer (VG Instruments, UK) with an Mg $K_\alpha$ X-ray source. Electron paramagnetic resonance (EPR) was obtained by an A300-10/12 (Bruker, Germany). Thermogravimetric (TG) analysis was measured on STA 449C (NETZSCH Corporation, Germany).

### 2.3. Adsorptive performance tests

Firstly, the model fuel was obtained by dissolving DBT in *n*-octane with the tetradecane as the internal standard. The initial sulfur concentrations in model fuel were 100, 200, 300, 500, and 800 mg·$L^{-1}$, respectively. The preparation process of the model fuel containing the 4,6-DMDBT was similar to the above, but the initial sulfur concentration was 425 mg·$L^{-1}$. The naphthalene or *para*-xylene (50 mg·$L^{-1}$) as competitive adsorbate was added into the model fuel containing the DBT (500 mg·$L^{-1}$ S).

Secondly, to investigate the adsorptive capacities of the as-prepared BN–2O materials, 20 mL of model fuel containing 0.05 g of adsorbent was shaken for *t* min and measured by Agilent 7890A gas chromatographs (Agilent Technologies, USA).

Finally, the dynamic adsorptive desulfurization experiments were conducted, and the calculation formula of adsorptive capacity, the linear form of the Langmuir model, the linear form of the Freundlich model, the linear form of the pseudo-first-order kinetic model, and the linear form of the pseudo-second-order kinetic model were enclosed in the supplemental information file in Appendix A [42,43].

## 3. Results and discussion

In this work, the cyanuric chloride and melamine were chosen as precursors to prepare polymer via a condensed method. For the fabrication of BN–2O, the boron acid and polymer precursors were pyrolyzed by boron thermal substitution of carbon atoms from the intermediates. As illustrated in Fig. 2(c), the condensation led to the formation of dual oxygen atoms doped BN. The morphology of as-prepared materials was observed by an electron microscope, and the results are displayed in Fig. 2(d). BN–2O presented the similar morphology to cotton (Fig. S1(a) in Appendix A), which could be formed through the polymerization of cyanuric chloride and melamine molecules. In sharp contrast, the as-fabricated BN–OH reference (Fig. S1(b) in Appendix A) exhibited typical nanowire structures. As confirmed by TEM analysis, the BN–2O sample (Fig. 2(d) and Appendix A Figs. S1(c) and (d)) revealed a flake-like morphology with porous structures consisting of the wrinkle of layers. Whereas the pore of BN–OH Fig. 2(b) only distributed in nanowires. Moreover, it can be noted that there was a slight difference in the crystal structure between BN–2O and BN–OH. XRD analysis (Fig. 2(e)) showed a broad peak at 23° corresponding to typical (002) patterns of BN [44,45]. However, the characteristic peak intensity at around 42° on BN–2O was slightly weaker than that of BN–OH. It suggested that the disordered atomic arrangements of the BN–2O samples might affect the electronic and surface structures [46].

The results of $N_2$ adsorption and desorption isotherms further verified the effect of polymerization and condensation (Fig. 2(f)). The specific surface areas were 1306 and 1309 $m^2 \cdot g^{-1}$ for BN–2O and BN–OH, respectively. The pore size of BN–2O was centered

at 0.93 nm (Fig. 2(g)), which could be originated from the decomposition of polymeric substances [47]. As shown in Fig. 2(f), BN–2O presented typical IV adsorption and desorption isotherms with characteristic H4-type hysteresis loop, and the adsorption was unsaturated at a high relative pressure ($P/P_0$), indicating the existence of mesopores, micropores, and macropores [48]. Noticeably, it matched well with the TEM observations. In addition, it is worth noticing that BN–2O exhibited a significant fraction of micropores smaller than 1 nm, which was very active in the adsorption process. Besides, the mesopores and macropores could also facilitate mass transfer [49–51]. Therefore, the hierarchically porous structure could be favorable for the adsorptive desulfurization process.

FTIR analysis depicted that condensation affected the final bonding nature of BN–2O (Figs. 3(a) and (b)). Several characteristic bands of the BN–OH samples were observed at 3408, 1387, and 799 $cm^{-1}$, corresponding to the vibration of B–OH, the in-plane B–N stretching vibrations, and out-of-plane B–N–B bending vibrations, respectively [39,52]. Compared with BN–OH, there was a new peak appeared at 1040 $cm^{-1}$ for BN–2O, which was assigned to the $sp^2$ hybridized B–O bond [53]. The UV–Vis DRS was collected to further understand the electronic structure of BN–2O (Fig. 3(c)). The optical absorptions were changed remarkably for BN–2O compared with that of BN–OH. As illustrated in Fig. 3(c), one characteristic absorption peak located at 247 nm was observed for the BN–OH and BN–2O, which could be ascribed to electron excitations of BN [54]. Another absorption peak of BN–2O at 320 nm was generated by vacancies and impurities [55]. The oxygen atom was embedded in the in-plane of BN–2O, and thereafter inducing the formation of unique electronic structures of BN–2O different with those of BN–OH. The higher electronegativity of the oxygen atom could serve as a polar center to enhance the π–π interaction of donor–acceptor between BN and electron-rich derivative of DBT [56]. XPS analysis was employed to get insight into the electronic structures of BN–2O and BN–OH (Figs. 3(d)–(f)). The detailed composition was summarized in Table S2 in Appendix A, and the results indicated a significant increase in the oxygen content, which might arise from the initial polymerization. To further investigate the chemical states of the elements, the B 1s peaks of BN–2O were deconvoluted into three peaks at around 190.8, 191.7, and 192.6 eV, which were attributed to the B–N, B–OH [57], and B–O [40], respectively. It was noted that BN–2O not only showed a higher concentration of B–OH structure than that of BN–OH, but also possessed a considerable number of B–O structures, as listed in Table S2. Moreover, the O 1s XPS of BN–2O displayed lower binding energy than that of BN–OH, indicating a higher concentration of interior substituted O in BN–2O. Through the oxygen doping strategy, the defect structure of BN–2O could be controllably modulated.

In order to directly identify the defect structure of the materials, we conducted EPR experiments (Fig. 4(a)). Compared with BN–OH, BN–2O showed a sharp signal of oxygen atom interior substitution in BN structure at $g = 2.0616$, which was derived from the existence of numerous paramagnetic defect structures and unpaired electrons [58]. All the above analyses apparently revealed that the oxygen atoms were effectively doped in the BN–2O via the polymer-based synthetic routes.

As the previous report highlighted that the monochlorotriazine-type intermediates and the nitrogen-enriched graphene sheet could be simultaneously formed in polymerization between cyanuric chloride and melamine at low temperature [59]. The carbon atom of intermediate was substituted by B(OH) moieties or single boron atoms [60]. Therefore, there is in-plane substitution and out-of-plane hydroxylation. Based on previous studies, the formation of B–N bonds from boric acid and intermediate needed to overcome the energy barrier to remove the hydroxyl boric acid and other organic groups in the polymer [39]. When the primary or secondary amine was employed, the energy barrier was significantly reduced under the calcination. However, for tertiary amine, the formation of B–N bonds needed to overwhelm a higher energy barrier to eliminate the organic groups in the tertiary amine. In this case, a part of B–O bonds was resided in the as-prepared BN adsorbent in the form of interior oxygen groups. In order to further explore the hypothesis, TG analyses of different precursors were performed (Fig. S2 in Appendix A), and the results indicated that the precursor of BN–2O could be decomposed at a higher temperature than that of BN–OH. The processes of polymerization and

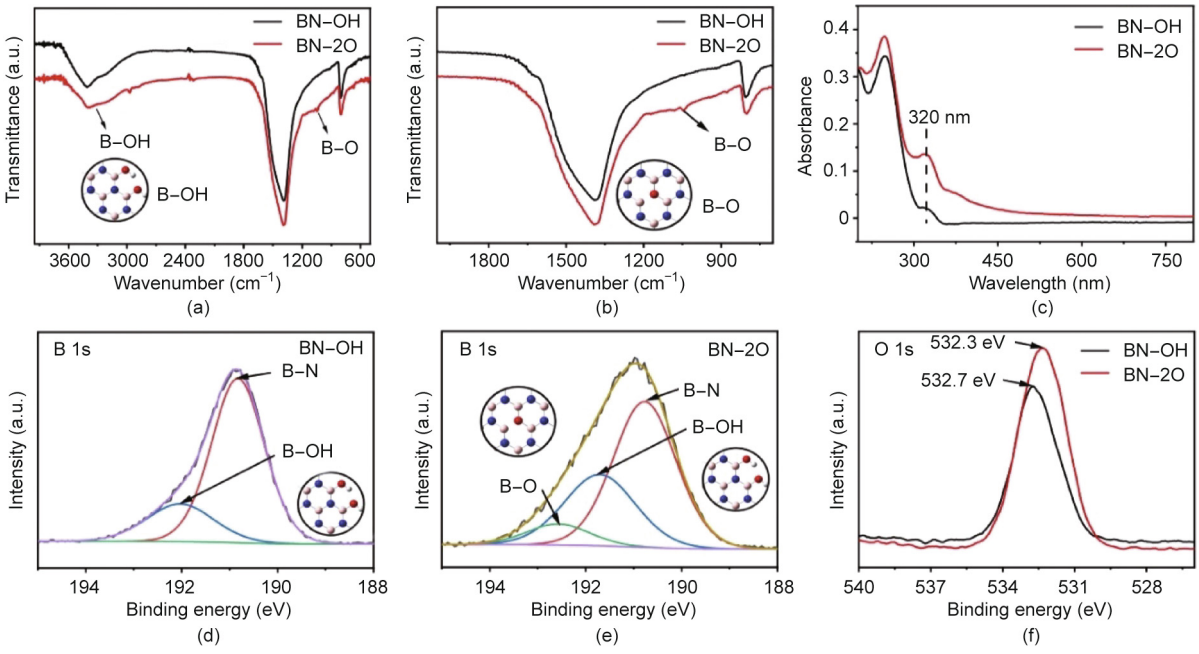


**Fig. 3.** (a, b) FTIR spectra of BN–OH and BN–2O. (c) UV–Vis DRS of BN–OH and BN–2O. (d–f) XPS spectra of the BN–OH and BN–2O: (d) BN–OH–B 1s; (e) BN–2O–B 1s; (f) O 1s. B–OH represents the out-of-plane edge hydroxylation of the boron atom, and B–O stands for the in-plane internal oxygen atom connected to the boron atom.

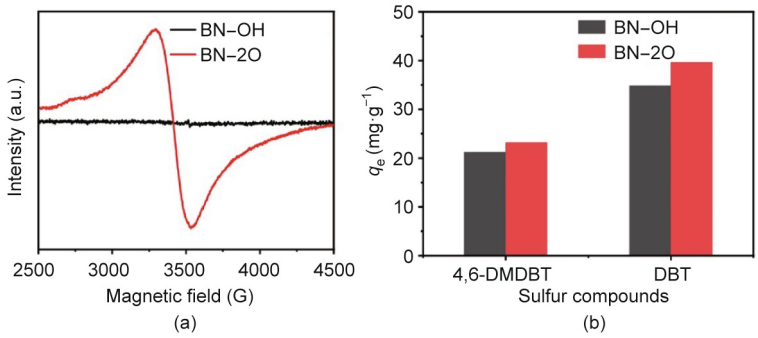


**Fig. 4.** (a) The EPR spectra of the BN–OH and BN–2O. (b) The different sulfur compounds of adsorptive capacities of different BN samples, $q_e$ (mg·g$^{-1}$): the amount of sulfur adsorbed at equilibrium. Experimental conditions: 500 mg·L$^{-1}$ initial sulfur concentration (DBT) and 425 mg·L$^{-1}$ initial sulfur concentration (4,6-DMDBT), *V*(fuel) = 20 mL, *m*(adsorbent) = 0.05 g, *T* = 298 K, atmospheric pressure.

condensation of the precursors on BN–2O could be confirmed, and the formation of B–N bonds from boric acid and intermediate required overcoming the energy barrier to remove the hydroxyl boric acid and other organic groups in the polymer. Therefore, it could be concluded that oxygen atom-scale interior substitution and edge hydroxylation in BN structures had been constructed via this polymer-based synthetic strategy.

Based on the above, BN–2O with a large portion of doped oxygen and a significant fraction of micropores was successfully constructed. Their properties endow the materials with compelling adsorptive desulfurization performance. The adsorptive desulfurization performance of BN–OH and BN–2O for DBT and 4,6-DMDBT removal were explored, and the results were depicted in Fig. 4(b). It was noted that BN–2O exhibited a distinctively higher adsorptive capacity than that of BN–OH. Moreover, the BN–2O adsorbent prepared in this work exhibited better adsorptive desulfurization performance than many reported adsorbents (Table S3 in Appendix A). To further investigate the difference of performance, two predominant factors, namely electronic properties and textures of materials, were taken into consideration [56]. On the one hand, based on $N_2$ adsorption and desorption isotherms and the pore size distribution result, BN–2O possessed a significant fraction of micropores smaller than 1 nm, which was very active in the adsorption process, and the mesopores and macropores structure could be beneficial to the improvement of adsorptive capacity [49,50,61]. On the other hand, BN–2O displayed a significant variety of oxygen atoms confined in BN edge and interior structures, resulting in enhanced interaction between the adsorbate and BN–2O.

To deeply understand how the doped oxygen in BN affects adsorptive desulfurization behaviors, we carried out the theoretical calculations. Based on density functional theory (DFT) calculation conducted on BN, BN–OH, and BN–2O (Fig. S3 in Appendix A), the adsorption of DBT molecule was investigated (Fig. 5). The doping number of oxygen atom interior substitution was defined as BN–2O$_x$ (*x* refers to the number of oxygen atom interior substitution). All models were optimized using the M062X-D3 method with dispersion correction in the 6-31G(d) basis set, and the adsorption free energies were calculated. It was found that the DBT was adsorbed on the BN model by a π–π interaction, and the adsorption free energy was −11.3 kcal·mol$^{-1}$ (1 kcal = 4.19002 × 10$^3$ J) (Fig. 5(b)). After edge hydroxylation, BN–OH owned enhanced adsorption of DBT with an adsorption free energy of −16.0 kcal·mol$^{-1}$ (Fig. 5(c)). Furthermore, the adsorption of DBT molecule on the BN–2O models were also studied (Figs. 5(d)–(f)). Due to the oxygen substitution in the interior of BN, the BN–2O models had the unpaired electron, which was corresponding to the result of EPR. However, the adsorption of DBT was hindered by the interior substituted oxygen. The adsorption free energies for the BN–2O$_1$, BN–2O$_2$, and BN–2O$_3$ models were −12.6, −12.8, and −13.4 kcal·mol$^{-1}$, respectively.

Natural population analysis (NPA) was employed to understand the mechanism of enhanced adsorption (Fig. S4 in Appendix A). Interestingly, after adsorption, the NPA charge distribution had less change on the DBT molecule except the S atom, on which the NPA charge increased. Owing to the higher electronegativity, the doped oxygen could withdraw electrons from the BN, reducing the electron density on the BN domain and thus promoting the π–π interaction between the adsorbent and adsorbate. Therefore, edge hydroxylation could increase the adsorptive capacity of the adsorbent (Scheme S1 in Appendix A). Because of this effect, BN–2O with more B–OH bonds could show higher capacity for the adsorption of aromatic sulfur.

The reason for the hindered adsorption of DBT on the BN–2O models was also investigated by the NPA charge analysis (Figs. S4(c)–(e) in Appendix A). Attractively, the charge distributions of adsorbed DBT molecules on the BN–2O models had been significantly affected. On the one hand, the interior substituted oxygen could work as a Lewis base site donating electrons to the conjugated ring of DBT molecule. On the other hand, the unsaturated boron could act as a Lewis acid site withdrawing electrons from the conjugated ring of DBT molecule. These two effects reduced the conjugation of DBT molecule, hindering the π–π interaction between the adsorbent and adsorbate. Moreover, it could also be noted that the DBT molecule tended to be far away from the interior substituted oxygen during the optimization of the DBT adsorbed BN–2O$_1$ model, indicating hindered π–π interaction by interior substituted oxygen (Fig. S5 in Appendix A). However, it should be noticed that the interior substituted oxygen in the BN–2O models could also increase the polarity of adsorbed DBT molecule, leading to a dipole interaction between the sulfur and oxygen. As investigated by NPA charge analysis, the charges at S atom of adsorbed DBT molecule on the BN–2O models were ordered as follows: BN–2O$_1$ (0.441) ≈ BN–2O$_2$ (0.439) < BN–2O$_3$ (0.456), same as the order of adsorption free energies: BN–2O$_1$ (−12.6 kcal·mol$^{-1}$) ≈ BN–2O$_2$ (−12.8 kcal·mol$^{-1}$) < BN–2O$_3$ (−13.4 kcal·mol$^{-1}$). This phenomenon indicated the contribution of dipole interaction to the adsorption of DBT molecule (Scheme S2 in Appendix A). Owing to this effect, BN–2O could selectively adsorb DBT from the aromatic-rich fuel.

Fig. S6 in Appendix A showed the results of competitive adsorptive capacity for the case with a certain number of aromatic hydrocarbons in the model fuel. Compared with the model fuels, in the presence of the naphthalene or *para*-xylene, the adsorptive capacities of BN–2O reached 32.4 and 33.6 mg S per gram of adsorbent, respectively. This result indicated the importance of interior substituted oxygen to the selective adsorption, corresponding to the result of theoretical calculation. More importantly, BN–2O still

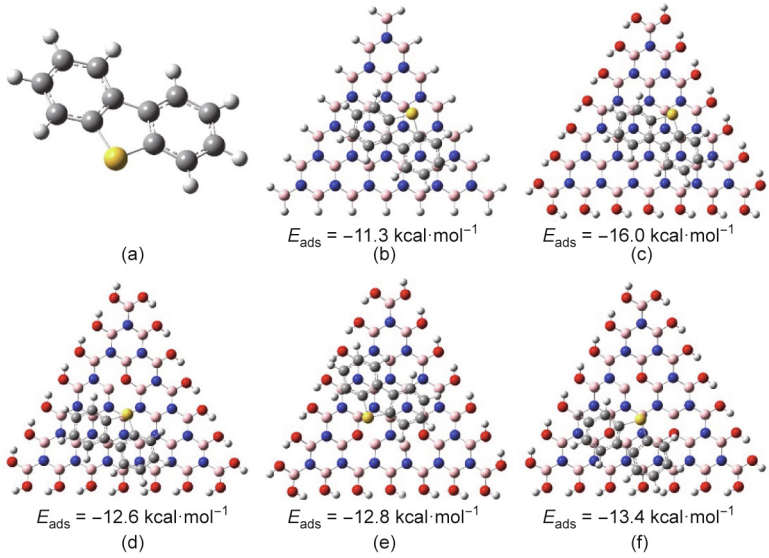


**Fig. 5.** (a) Molecular structure of DBT. The adsorption models of DBT on (b) BN, (c) BN–OH, (d) BN–2O$_1$, (e) BN–2O$_2$, and (f) BN–2O$_3$.

exhibited ultrahigh absorption performance. The adsorption of DBT on BN–2O from the model fuel with various initial concentrations was studied at room temperature (Fig. 6(a)) with high concentration, the adsorptive capacity of BN–2O was relatively high, which means initial concentration plays a crucial role in the adsorptive process. From the results described above, Langmuir and Freundlich isotherms were used to describe the adsorptive experimental data of DBT (Fig. 6(b) and Table S4 in Appendix A). The adsorptive result was well-fitted with the Freundlich model. In this model, the DBT was assumed to undergo multi-molecular layer type coverage of the DBT on the BN–2O uneven surface [62].

The adsorption kinetics of the DBT on BN–2O was also investigated in order to study the adsorption rate until the equilibrium was reached (Fig. 6(c) and Fig. S7 and Table S5 in Appendix A). Pseudo-first-order and pseudo-second-order models were used to determine adsorption behaviors. The pseudo-second-order kinetic coefficient ($R^2$) of BN–2O was closer to 1. The $h$ value at high initial concentration was still higher than that at low initial concentration, suggesting initial DBT concentration had a prominent effect on adsorption rate [63].

Fig. 6(d) depicted the dynamic adsorptive desulfurization performance of BN–2O. BN–2O exhibited higher adsorptive desulfurization performance, which should be attributed to its unique electronic structure and hierarchically porous structure. After being washed with toluene, BN–2O was dried for the next adsorptive desulfurization recycle, and the adsorptive capacity was well

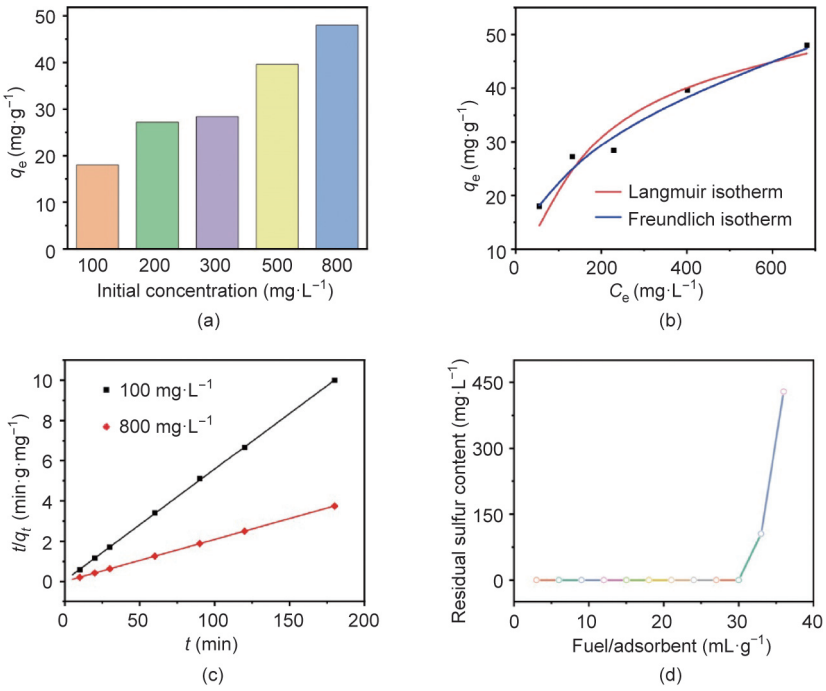


**Fig. 6.** (a) The effect of DBT with different sulfur initial concentrations on DBT adsorptive capacity of BN–2O. (b) Langmuir and Freundlich isotherms of DBT adsorbed on BN–2O. (c) The pseudo-second-order adsorption kinetics of BN–2O as an adsorbent for the removal of DBT. $C_e$ (mg·L$^{-1}$): equilibrium concentration; $q_t$ (mg·g$^{-1}$): adsorption capacity at $t$ min. Experimental conditions: $V$(fuel) = 20 mL, $m$(adsorbent) = 0.05 g, $T$ = 298 K, atmospheric pressure. (d) DBT breakthrough adsorption curve of BN–2O.

in accordance with earlier adsorptive desulfurization performance after four cycles. The adsorptive capacity was 39.6, 31.2, 27.6, and 24.4 mg S per gram of adsorbent, respectively. Therefore, the present materials have potential application perspectives for adsorptive desulfurization technology.

## 4. Conclusions

Herein, we present oxygen atoms doped BN lattice fabricated by the mixture pyrolysis of boric acid and polymer originated from the condensation of cyanuric chloride and melamine molecules. Compared with BN–OH, the adsorptive capacity of the as-prepared BN–2O sample was significantly improved due to its rich oxygen content and micropores. The DBT was assumed to undergo multi-molecular layer type coverage on the BN–2O uneven surface. As revealed by the theoretical calculation, the dual oxygen simultaneous modification could provide improved adsorptive desulfurization performance to the BN–2O adsorbent. The adsorptive capacity of BN–2O was in well accordance with earlier adsorptive desulfurization performance after four cycles. Therefore, we suggest the BN–2O material as a highly efficient adsorbent for adsorptive desulfurization. This work provides an insight into the controllable synthesis of BN–2O, leading to a great prospect to the design and application of heteroatom-doped adsorbent materials.

## Acknowledgments

This work was financially supported by the National Key Research and Development Program of China (2017YFB0306504), the National Natural Science Foundation of China (22178154, 22108105, 21722604, and 21878133), the Postdoctoral Foundation of China (2017M611726), and Graduate Education Innovation Project of Government of Jiangsu Province (KYCX20_3039).

## Compliance with ethics guidelines

Jing Luo, Yanchen Wei, Yanhong Chao, Chao Wang, Hongping Li, Jun Xiong, Mingqing Hua, Huaming Li, and Wenshuai Zhu declare that they have no conflict of interest or financial conflicts to disclose.

## Appendix A. Supplementary data

Supplementary data to this article can be found online at https://doi.org/10.1016/j.eng.2020.08.030.

## References

[1] Laredo GC, Vega Merino PMV, Hernández PS. Light cycle oil upgrading to high quality fuels and petrochemicals: a review. Ind Eng Chem Res 2018;57(22):7315–21.
[2] Cao Z, Zhang X, Xu C, Huang X, Wu Z, Peng C, et al. Selective hydrocracking of light cycle oil into high-octane gasoline over bi-functional catalysts. J Energy Chem 2021;52:41–50.
[3] Yang C, Li R, Cui C, Liu S, Qiu Q, Ding Y, et al. Catalytic hydroprocessing of microalgae-derived biofuels: a review. Green Chem 2016;18(13):3684–99.
[4] Stanislaus A, Marafi A, Rana MS. Recent advances in the science and technology of ultra low sulfur diesel (ULSD) production. Catal Today 2010;153(1–2):1–68.
[5] Zhang M, Liu J, Yang J, Chen X, Wang M, Li H, et al. Molybdenum-containing dendritic mesoporous silica spheres for fast oxidative desulfurization in fuel. Inorg Chem Front 2019;6(2):451–8.
[6] Wang C, Qiu Y, Wu HY, Yang WS, Zhu Q, Chen ZG, et al. Construction of 2D–2D $V_2O_5$/BNNS nanocomposites for improved aerobic oxidative desulfurization performance. Fuel 2020;270:117498.
[7] Zhu W, Wang C, Li H, Wu P, Xun S, Jiang W, et al. One-pot extraction combined with metal-free photochemical aerobic oxidative desulfurization in deep eutectic solvent. Green Chem 2015;17(4):2464–72.
[8] Jiang W, Jia H, Li H, Zhu L, Tao R, Zhu W, et al. Boric acid-based ternary deep eutectic solvent for extraction and oxidative desulfurization of diesel fuel. Green Chem 2019;21(11):3074–80.
[9] Jiang W, Zhu K, Li HP, Zhu LH, Hua MQ, Xiao J, et al. Synergistic effect of dual Brønsted acidic deep eutectic solvents for oxidative desulfurization of diesel fuel. Chem Eng J 2020;394:124831.
[10] Bhadra BN, Jhung SH. Well-dispersed Ni or MnO nanoparticles on mesoporous carbons: preparation via carbonization of bimetallic MOF-74s for highly reactive redox catalysts. Nanoscale 2018;10(31):15035–47.
[11] Almashjary KH, Khalid M, Dharaskar S, Jagadish P, Walvekar R, Gupta TCSM. Optimisation of extractive desulfurization using choline chloride-based deep eutectic solvents. Fuel 2018;234:1388–400.
[12] Wagle DV, Zhao H, Deakyne CA, Baker GA. Quantum chemical evaluation of deep eutectic solvents for the extractive desulfurization of fuel. ACS Sustain Chem Eng 2018;6(6):7525–31.
[13] Iravani AA, Gunda K, Ng FTT. Adsorptive removal of refractory sulfur compounds by tantalum oxide modified activated carbons. AIChE J 2017;63(11):5044–53.
[14] Ren X, Liu Z, Dong L, Miao G, Liao N, Li Z, et al. Dynamic catalytic adsorptive desulfurization of real diesel over ultra-stable and low-cost silica gel-supported $TiO_2$. AIChE J 2018;64(6):2146–59.
[15] Han Y, Sinnwell MA, Teat SJ, Sushko ML, Bowden ME, Miller QRS, et al. Desulfurization efficiency preserved in a heterometallic MOF: synthesis and thermodynamically controlled phase transition. Adv Sci 2019;6(7):1802056.
[16] Khan NA, An HJ, Yoo DK, Jhung SH. Polyaniline-derived porous carbons: remarkable adsorbent for removal of various hazardous organics from both aqueous and non-aqueous media. J Hazard Mater 2018;360:163–71.
[17] Sarker M, An HJ, Yoo DK, Jhung SH. Nitrogen-doped porous carbon from ionic liquid@Al–metal–organic framework: a prominent adsorbent for purification of both aqueous and non-aqueous solutions. Chem Eng J 2018;338:107–16.
[18] Qin JX, Tan P, Jiang Y, Liu XQ, He QX, Sun LB. Functionalization of metal–organic frameworks with cuprous sites using vapor-induced selective reduction: efficient adsorbents for deep desulfurization. Green Chem 2016;18(11):3210–5.
[19] Zhu W, Wu Z, Foo GS, Gao X, Zhou M, Liu B, et al. Taming interfacial electronic properties of platinum nanoparticles on vacancy-abundant boron nitride nanosheets for enhanced catalysis. Nat Commun 2017;8(1):15291.
[20] Zhu W, Gao X, Li Q, Li H, Chao Y, Li M, et al. Controlled gas exfoliation of boron nitride into few-layered nanosheets. Angew Chem Int Ed 2016;55(36):10766–70.
[21] Chao YH, Pang JY, Bai Y, Wu PW, Luo J, He J, et al. Graphene-like BN@$SiO_2$ nanocomposites as efficient sorbents for solid-phase extraction of rhodamine B and rhodamine 6G from food samples. Food Chem 2020;320:126666.
[22] Pakdel A, Bando Y, Golberg D. Nano boron nitride flatland. Chem Soc Rev 2014;43(3):934–59.
[23] Lu L, He J, Wu P, Wu Y, Chao Y, Li H, et al. Taming electronic properties of boron nitride nanosheets as metal-free catalysts for aerobic oxidative desulfurization of fuels. Green Chem 2018;20(19):4453–60.
[24] Wu P, Zhu W, Chao Y, Zhang J, Zhang P, Zhu H, et al. A template-free solvent-mediated synthesis of high surface area boron nitride nanosheets for aerobic oxidative desulfurization. Chem Commun 2016;52(1):144–7.
[25] Ling Z, Wang Z, Zhang M, Yu C, Wang G, Dong Y, et al. Sustainable synthesis and assembly of biomass-derived B/N Co-doped carbon nanosheets with ultrahigh aspect ratio for high-performance supercapacitors. Adv Funct Mater 2016;26(1):111–9.
[26] Chen S, Chen Z, Siahrostami S, Higgins D, Nordlund D, Sokaras D, et al. Designing boron nitride islands in carbon materials for efficient electrochemical synthesis of hydrogen peroxide. J Am Chem Soc 2018;140(25):7851–9.
[27] Pang J, Chao Y, Chang H, Li H, Xiong J, Zhang Q, et al. Silver nanoparticle-decorated boron nitride with tunable electronic properties for enhancement of adsorption performance. ACS Sustain Chem Eng 2018;6(4):4948–57.
[28] Chao YH, Zhang J, Li HP, Wu PW, Li XW, Chang HH, et al. Synthesis of boron nitride nanosheets with N-defects for efficient tetracycline antibiotics adsorptive removal. Chem Eng J 2020;387:124138.
[29] Xiong J, Zhu WS, Li HP, Yang L, Chao YH, Wu PW, et al. Carbon-doped porous boron nitride: metal-free adsorbents for sulfur removal from fuels. J Mater Chem A 2015;3(24):12738–47.
[30] Nag A, Raidongia K, Hembram KPSS, Datta R, Waghmare UV, Rao CNR. Graphene analogues of BN: novel synthesis and properties. ACS Nano 2010;4(3):1539–44.
[31] Yan Z, Lin J, Yuan X, Song T, Yu C, Liu Z, et al. Desulfurization of model oil by selective adsorption over porous boron nitride fibers with tailored microstructures. Sci Rep 2017;7(1):3297.
[32] Kinaci A, Haskins JB, Sevik C, Cagin T. Thermal conductivity of BN–C nanostructures. Phys Rev B 2012;86(11):115410.
[33] D'yachkov EP, D'yachkov PN. Electronic structure of doped boron nitride nanotubes as potential catalysts of photochemical water splitting. Russ J Inorg Chem 2018;63(9):1204–10.
[34] Huang C, Chen C, Zhang M, Lin L, Ye X, Lin S, et al. Carbon-doped BN nanosheets for metal-free photoredox catalysis. Nat Commun 2015;6(1):7698.
[35] Chen SR, Li P, Xu ST, Pan XL, Fu Q, Bao XH. Carbon doping of hexagonal boron nitride porous materials toward $CO_2$ capture. J Mater Chem A 2018;6(4):1832–9.

[36] Pang J, Chao Y, Chang H, Li H, Xiong J, He M, et al. Tuning electronic properties of boron nitride nanoplate via doping carbon for enhanced adsorptive performance. J Colloid Interface Sci 2017;508:121–8.
[37] Lu Q, Zhao Q, Yang TY, Zhai CB, Wang DX, Zhang MZ. Preparation of boron nitride nanoparticles with oxygen doping and a study of their room-temperature ferromagnetism. ACS Appl Mater Interfaces 2018;10(15):12947–53.
[38] Lei W, Zhang H, Wu Y, Zhang B, Liu D, Qin S, et al. Oxygen-doped boron nitride nanosheets with excellent performance in hydrogen storage. Nano Energy 2014;6:219–24.
[39] Weng Q, Kvashnin DG, Wang X, Cretu O, Yang Y, Zhou M, et al. Tuning of the optical, electronic, and magnetic properties of boron nitride nanosheets with oxygen doping and functionalization. Adv Mater 2017;29(28):1700695.
[40] Liu F, Li S, Yu DF, Su YP, Shao NN, Zhang ZT. Template-free synthesis of oxygen-doped bundlelike porous boron nitride for highly efficient removal of heavy metals from wastewater. ACS Sustain Chem Eng 2018;6(12):16011–20.
[41] Xiong J, Yang L, Chao Y, Pang J, Zhang M, Zhu W, et al. Boron nitride mesoporous nanowires with doped oxygen atoms for the remarkable adsorption desulfurization performance from fuels. ACS Sustain Chem Eng 2016;4(8):4457–64.
[42] Qu Z, Wu Y, Zhu S, Yu Y, Huo M, Zhang L, et al. Green synthesis of magnetic adsorbent using groundwater treatment sludge for tetracycline adsorption. Engineering 2019;5(5):880–7.
[43] Bagali SS, Gowrishankar BS, Roy AS. Optimization, kinetics, and equilibrium studies on the removal of lead (II) from an aqueous solution using banana pseudostem as an adsorbent. Engineering 2017;3(3):409–15.
[44] Song Q, Liang J, Fang Yi, Cao C, Liu Z, Li L, et al. Selective adsorption behavior/mechanism of antibiotic contaminants on novel boron nitride bundles. J Hazard Mater 2019;364:654–62.
[45] Li Y, Tian X, Yang W, Li Q, Hou L, Zhu Z, et al. Dielectric composite reinforced by *in-situ* growth of carbon nanotubes on boron nitride nanosheets with high thermal conductivity and mechanical strength. Chem Eng J 2019;358:718–24.
[46] Luo J, Xiong J, Chao Y, Li X, Li H, Pang J, et al. Activated boron nitride ultrathin nanosheets for enhanced adsorption desulfurization performance. J Taiwan Inst Chem Eng 2018;93:245–52.
[47] Gautam C, Tiwary CS, Jose S, Brunetto G, Ozden S, Vinod S, et al. Synthesis of low-density, carbon-doped, porous hexagonal boron nitride solids. ACS Nano 2015;9(12):12088–95.
[48] Luo J, Chao Y, Tang Z, Hua M, Li X, Wei Y, et al. Design of Lewis acid centers in bundlelike boron nitride for boosting adsorptive desulfurization performance. Ind Eng Chem Res 2019;58(29):13303–12.
[49] Shi YW, Zhang XW, Liu GZ. Activated carbons derived from hydrothermally carbonized sucrose: remarkable adsorbents for adsorptive desulfurization. ACS Sustain Chem Eng 2015;3(9):2237–46.
[50] Seredych M, Lison J, Jans U, Bandosz TJ. Textural and chemical factors affecting adsorption capacity of activated carbon in highly efficient desulfurization of diesel fuel. Carbon 2009;47(10):2491–500.
[51] Chen X, Zhang M, Wei Y, Li H, Liu J, Zhang Q, et al. Ionic liquid-supported 3DOM silica for efficient heterogeneous oxidative desulfurization. Inorg Chem Front 2018;5(10):2478–85.
[52] Moon OM, Kang BC, Lee SB, Boo JH. Temperature effect on structural properties of boron oxide thin films deposited by MOCVD method. Thin Solid Films 2004;464:164–9.
[53] Weng Q, Ide Y, Wang X, Wang X, Zhang C, Jiang X, et al. Design of BN porous sheets with richly exposed (002) plane edges and their application as $TiO_2$ visible light sensitizer. Nano Energy 2015;16:19–27.
[54] Li H, Zhu S, Zhang M, Wu P, Pang J, Zhu W, et al. Tuning the chemical hardness of boron nitride nanosheets by doping carbon for enhanced adsorption capacity. ACS Omega 2017;2(9):5385–94.
[55] Xiong J, Yang L, Chao Y, Pang J, Wu P, Zhang M, et al. A large number of low coordinated atoms in boron nitride for outstanding adsorptive desulfurization performance. Green Chem 2016;18(10):3040–7.
[56] Tan P, Xue DM, Zhu J, Jiang Y, He QX, Hou ZF, et al. Hierarchical N-doped carbons from designed N-rich polymer: adsorbents with a record-high capacity for desulfurization. AIChE J 2018;64(11):3786–93.
[57] Lee D, Lee B, Park KH, Ryu HJ, Jeon S, Hong SH. Scalable exfoliation process for highly soluble boron nitride nanoplatelets by hydroxide-assisted ball milling. Nano Lett 2015;15(2):1238–44.
[58] Lv C, Qian Y, Yan C, Ding Y, Liu Y, Chen G, et al. Defect engineering metal-free polymeric carbon nitride electrocatalyst for effective nitrogen fixation under ambient conditions. Angew Chem Int Ed 2018;57(32):10246–50.
[59] Yang SJ, Cho JH, Oh GH, Nahm KS, Park CR. Easy synthesis of highly nitrogen-enriched graphitic carbon with a high hydrogen storage capacity at room temperature. Carbon 2009;47(6):1585–91.
[60] Weng Q, Wang B, Wang X, Hanagata N, Li X, Liu D, et al. Highly water-soluble, porous, and biocompatible boron nitrides for anticancer drug delivery. ACS Nano 2014;8(6):6123–30.
[61] Liu FJ, Huang K, Wu Q, Dai S. Solvent-free self-assembly to the synthesis of nitrogen-doped ordered mesoporous polymers for highly selective capture and conversion of $CO_2$. Adv Mater 2017;29(27):1700445.
[62] Chang H, Chao Y, Pang J, Li H, Lu L, He M, et al. Advanced overlap adsorption model of few-layer boron nitride for aromatic organic pollutants. Ind Eng Chem Res 2018;57(11):4045–51.
[63] Xiong J, Zhu W, Li H, Ding W, Chao Y, Wu P, et al. Few-layered graphene-like boron nitride induced a remarkable adsorption capacity for dibenzothiophene in fuels. Green Chem 2015;17(3):1647–56.